In Operando X-ray Diffraction Strain Measurement in Ni_3Sn_2 – Coated Inverse Opal Nanoscaffold Anodes for Li-ion Batteries

Matthew P. B. Glazer[1,2], Junjie Wang[3], Jiung Cho[3,4], Jonathan D. Almer[5], John S. Okasinski[5], Paul V. Braun[3], and David C. Dunand[1*]

[1]*Department of Materials Science and Engineering, Northwestern University, Evanston, IL 60208, USA.*
[2]*Materials and Corrosion Engineering Practice, Exponent, Inc., Menlo Park, CA, 94025, USA.*
[3]*Department of Materials Science and Engineering, University of Illinois at Urbana-Champaign, Champaign, IL 61801, USA.*
[4]*Gangneung Center, Korea Basic Science Institute, Gangneung, 210-702, Republic of Korea*
[5]*X-ray Science Division, Argonne National Laboratory, Argonne, IL 60439, USA.*

* Correspondence can be addressed to D.C.D. at dunand@northwestern.edu
Phone: +1 (847) 491 - 5370 Fax: +1 (847) 491 - 7820

Abstract

Volume changes associated with the (de)lithiation of a nanostructured Ni_3Sn_2 coated nickel inverse opal scaffold anode create mismatch stresses and strains between the Ni_3Sn_2 anode material and its mechanically supporting Ni scaffold. Using *in operando* synchrotron x-ray diffraction measurements, elastic strains in the Ni scaffold are determined during cyclic (dis)charging of the Ni_3Sn_2 anode. These strains are characterized using both the center position of the Ni diffraction peaks, to quantify the average strain, and the peak breadth, which describes the distribution of strain in the measured volume. Upon lithiation (half-cell discharging) or delithiation (half-cell charging), compressive strains and peak breadth linearly increase or decrease, respectively, with charge. The evolution of the average strains and peak breadths suggests that some irreversible plastic deformation and/or delamination occurs during cycling, which can result in capacity fade in the anode. The strain behavior associated with cycling of the Ni_3Sn_2 anode is similar to that observed in recent studies on a Ni inverse-opal supported amorphous Si anode and demonstrates that the (de)lithiation-induced deformation and damage

mechanisms are likely equivalent in both anodes, even though the magnitude of mismatch strain in the Ni_3Sn_2 is lower due to the lower (de)lithiation-induced contraction/expansion.

Keywords: Tin Anodes, In Operando, Lithiation Strain, Intermetallic Alloying Anode, Microbattery

1. Introduction

Lithium-ion batteries (LIBs) are versatile energy storage devices, however, there is a continuing demand for significantly faster charging times and higher energy densities [1–4]. Materials that alloy with lithium, such as tin compounds, are promising candidates for increasing both the power and energy density of LIBs, with a theoretical capacity up to 2.7 times greater than that of conventionally utilized graphite (994 mAh/g for pure Sn vs 372 mAh/g for graphite [5]). However, Sn undergoes a very large volume expansion (> 260%) during lithiation, which generates large stresses that can, with repeated cycling, cause cracking, pulverization and delamination in Sn-based anodes, leading to rapid capacity fade and failure [5].

Nanostructured and composite anode approaches have been well explored in the literature [6–10] as a means of reversibly accommodating these large volume changes, with many of the strategies utilized being borrowed from research into silicon-based alloying anodes [7]. Reducing the dimensions and the relevant size scales of Sn-based anode geometries is one strategy used to reduce the maximum stresses developed during lithiation [5,6] but is highly dependent on what Li-Sn phases may form during the lithiation process. Xu et al. observed that cracks form in pure Sn nanoparticles even at sizes as small as 10 nm, which are likely caused by sharp phase transformations [11], and demonstrated that shrinking the size of Sn nanoparticles alone is not entirely effective in eliminating damage accumulation during cycling. Composite Sn-based anode approaches, with either inactive matrices (such as Ni or Li_2O) or active matrices (such as

Si or Sb) are also effective at reducing the maximum stress and inelastic deformation [5,12–16]. Additionally, by employing composite anode materials, it is possible to increase the overall energy density while maintaining the same amount of lithiation-induced stresses and strains due to the decrease in lithiation voltage in comparison to pure Sn [16]. While many of these approaches have proven effective in increasing useable capacity or cycle-life, quantifying the lithiation-induced stresses that develop during cycling should enable the more rigorous design of high capacity, long-lived Sn-based anodes.

To begin to understand lithiation-induced strains and stresses in Sn-based anodes during cycling, *in operando* studies have been performed on simple geometries [17–24]. Using TEM, AFM, optical laser measurement techniques and transmission x-ray microscopy (TXM), researchers have measured strain, and observed phase transitions, microstructural changes and crack growth *in operando*. TEM and TXM studies have recorded the propagation of lithiation reaction fronts and the growth of cracks *in operando* while at the same time estimating strain in single particles, nanowires or other geometries [17,21–23,25,26]. Using optical laser measurement techniques, plastic deformation was quantified *in situ* in a coated thin film, which may be linked to discrete phase transitions occurring during lithiation [17]. While these methods are able to characterize strain and phase transitions in simple geometries *in situ/operando*, they cannot directly measure the spatial distribution of stresses and strains in more complex, nanostructured geometries as well as bulk material behavior, especially for commercially relevant anode geometries.

X-ray diffraction (XRD) based strain measurements are capable of directly measuring elastic strain distributions in arbitrary geometries and bulk materials *in operando* [27–30].. By observing changes in diffraction peak position, width and shape, one can characterize elasto-

plastic deformation in a given materials system. XRD has been used to identify different Li-Sn phases and quantify phase composition of various Sn-based anodes *in situ* [14,31], and *in operando* [32–34], but none have yet employed XRD to measure strain in nanostructured Sn-based alloying anodes.

In the present study, we employ synchrotron-based X-ray diffraction to characterize strains *in operando* in an intermetallic Sn-based, Li-alloying anode during several charging/discharging cycles. We measure mismatch strains that develop during (de)lithiation between the supporting inactive nanostructured inverse opal nickel scaffold and the Ni_3Sn_2 anode coating (or Ni_3Sn_2 anode) at even time intervals and at three different locations in the anode during galvanostatic cycling. As in previous studies in a similar nanostructured Si-based inverse opal anode [30], where the Si did not diffract, no Ni_xSn_y phases were observed to diffract, thus mismatch strains were measured in the nickel scaffold only. The results of this study are compared to [30] and are discussed in terms of elasto-plastic deformation and damage within the scaffold and active material.

2 Experimental

2.1 Electrode Fabrication

The fabrication of bicontinuous inverse opal nickel supported nickel-tin battery anodes is described in detail by Pikul et al. [35]. Briefly, to create a 10 μm thick opal template structure, 500 nm polystyrene (PS) spheres are self-assembled onto a gold-coated soda-lime silica glass substrate. After the PS spheres are sintered at a temperature near 96°C, which strengthens and slightly densifies the template, Ni is electrodeposited into the void space between the template spheres. Tetrahydrofuran is then used to remove the template spheres and reveal an interconnected inverse opal scaffold with nodes and struts. The scaffold is then electropolished to

decrease its relative density, before a thin film (~30-50 nm) of nickel-tin alloy (Ni_3Sn_2) active layer is electrodeposited onto the scaffold surfaces. The porosity of the as fabricated electrode is estimated to be 38-50% based on geometric calculations in Glazer et al. [30], with an approximate volume ratio between Ni_3Sn_2 and Ni of 0.9:1 to 1.4:1. The final electrode morphology appears similar to the representative SEM micrograph shown in Figure 1 and Figure S1 collected on a Hitachi S4800 SEM.

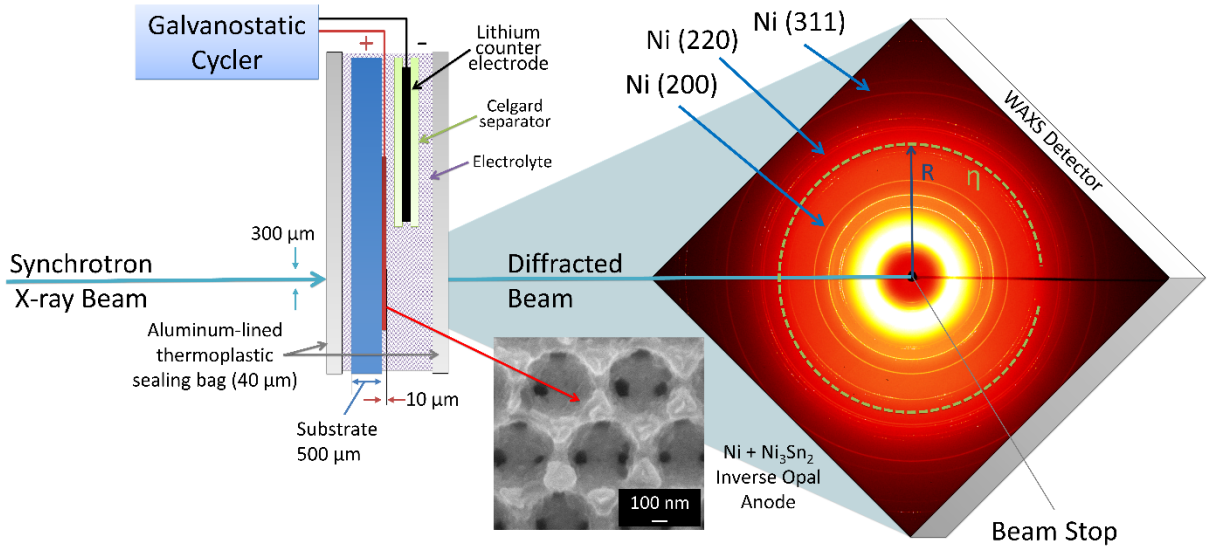

Figure 1: Schematic of *in operando* x-ray diffraction based strain measurements.

2.2 Electrochemical Cell Fabrication

An electrochemical pouch cell was fabricated to enable *in operando* x-ray diffraction measurements of the Ni supported Ni_3Sn_2 anode as shown in Figure 1. The anode was connected to an external Ni tab that was in contact with the gold coating on the substrate. A Celgard 2500 polypropylene separator was wrapped around a 380 µm thick metallic lithium counter-electrode, which was placed out of the path of the x-ray beam at least 5mm away from the anode. Both electrodes and the separator were immersed in 1M $LiClO_4$ dissolved in a 1:1 mixture of ethylene

carbonate and dimethylene carbonate and sealed in a polyamide-coated aluminum pouch while inside of an argon-filled glove box.

2.3 In Operando X-ray Diffraction Measurements

In operando x-ray diffraction measurements were collected at the Advanced Photon Source, (APS, Argonne National Laboratory, IL, USA), using the beam line station 17-BM. A monochromatic x-ray beam (E = 17.0 keV, λ = 0.07291 nm) 300 μm diameter shined on the sample in a transmission geometry through the thickness of the electrochemical cell at three different points. While the position of the x-ray beam was constant, an undesired x-ray beam energy drift from the nominal 17 keV value was observed during the experiment that affected the raw x-ray data and will be discussed later. Each point represents a total diffracting volume of ~$7x10^5$ μm^3 or up to 10^6 inverse opal unit cells. As shown schematically in Figure 1, x-rays passing through the nickel scaffold, glass substrate and polyamide coated aluminum pouch walls generated Debye-Scherrer diffraction rings wherever the Ni scaffold crystals satisfied the Bragg condition. The electrochemical cell was translated relative to the fixed x-ray beam every five minutes, cycling between volumes I, II, and III along a single line, resulting in 15 minutes elapsing between the collection of three diffraction patterns from three different volumes in the same anode. The distance between volumes I and II, and II and III was approximately 1mm from center to center, with the distance between volumes I and III approximately 2mm from center to center. At each point, transmitted diffraction rings were recorded with a 30 s exposure time onto an a-Si PerkinElmer 2048 x 2048 pixel area detector with a 200 x 200 μm pixel size and a 16-bit dynamic range placed at 250 mm from the sample. A powder sample of LaB_6 (NIST SRM-660b) was measured separately prior to *in operando* measurements and used as a reference to

determine the geometry of the instrument and experimental setup, sample to detector distance and to provide a calibration standard for the instrumental and geometric peak breadth.

2.4 Electrochemical Measurements

The electrochemical cell was precycled *ex situ* using a Bio-logic VMP3 battery cycler with a voltage window of 1.5 V to 50 mV (vs. Li/Li^+) and current of 268 mA/g, corresponding to a rate of ~0.3 C (i.e., one charge every three hours) for two full lithiation-delithiation cycles and one lithiation step interrupted at 439 mAh/g after 98 minutes of lithiation. The precycled cell was then cycled *in operando* by first completing the interrupted lithiation step from precycling, using a Maccor 4300 battery cycler, while exposed to x-ray radiation. The cell was then measured *in operando* using the same voltage window and a current of 404 mA/g, or a rate of 0.8 C, for six cycles. The amount of electrochemically active Ni_3Sn_2 alloy in the inverse opal anode was calculated to be 372 μg from the initial precycling delithiation capacity of the cell in comparison with a typical half-cell delithiation voltage vs. capacity curve and an overall delithiation capacity of 728.5 mAh/g as described in [35]. The *in operando* electrochemical measurements were matched with the corresponding diffraction pattern by correlating the time stamps between the two data sets. Additional electrochemical data is included in the supplemental materials (see Figures S2 and S3 and Table S1).

2.5 Fitting of Diffraction Patterns

Diffraction peaks from the nickel inverse opal scaffold were fit to pseudo-Voight functions to determine the peak intensities, widths and center positions. The latter were used to compute the lattice strains present in the scaffold during electrochemical cycling. Calibration parameters, such as sample to detector distance and beam center, were determined using FIT2D [36,37] from the LaB_6 diffraction pattern collected nominally under the same conditions as the *in operando*

cycling. Lattice strains from the measured nickel diffraction rings, Ni (200), (220) and (311), were determined using MATLAB programs developed at the APS as described in [27–30]. Each Ni diffraction ring over the measured 360 degree azimuthal angle from the area detector was divided into 10° azimuthal slices and fit independently in each slice. The pseudo-Voight shape fitting parameters for 35 out of 36 possible sections were averaged to describe the in-plane average lattice spacing and the full width half maximum (FWHM) of the peak under examination (one section was omitted due to the beam-stop support shadow on the detector).

2.6 Background and Instrumental Corrections

Although the experiment was initially performed at 17.0 keV with beam parameters calibrated using a LaB_6 standard, an instrument-related energy drift occurred during the experiment, principally attributed to a re-equilibration of the beam-line after a loss of beam. This energy drift resulted in both dramatic decreases in Ni and Al diffraction peak intensities (see Figures S4 and S5 respectively), as well as concomitant changes in apparent lattice spacing in both the Ni diffraction peaks and the Al pouch wall diffraction peaks, (see Figure S6 for as measured Ni (200) lattice spacings and Figure S7 for Al diffraction peak shifts) throughout the experiment. The shifts in lattice spacing in all diffraction patterns associated with the energy drift were fit and accounted for using the Al diffraction rings measured in the pattern as a reference, as the Al was expected to remain inert during cycling due to the polyamide coating separating the electrolyte from the Al foils. Details regarding the energy drift correction are available in Table S2 and the supplemental materials.

The Ni peak FWHMs observed appeared consistent both with expectations of strain distributions and with our previous work examining broadening in inverse opal anode systems [30]. Measured Ni FWHMs include geometrical and instrumental broadening contributions in

addition to the actual width of the Ni peaks. To correct for the instrumental and geometrical contributions, the LaB_6 peak width was assumed to represent the instrumental contribution only, in accordance with its designation as a diffraction line standard material (NIST SRM-660b). In a procedure identical to that described in [30], the measured LaB_6 FWHMs were fit as a function of sin(θ) and subtracted from the measured Ni FWHM using the following equation:

$$FWHM_{Ni} = \sqrt{FWHM_{Meas}^2 - (A * \sin(\theta) + B)^2} \quad (1)$$

where A and B are 2.7295 and 2.4058 respectively. For all volumes studied, the three Ni peak FWHMs were found to have be non-linear versus sin(θ). A linear relationship between FWHM and sin(θ) is needed to separate the size and microstrain contributions using the Williamson Hall method [30]. Such non-linearity has been previously observed in Ni coatings and treated using a modified Williamson Hall method [38–40]. However due to the fact that only three non-overlapped peaks were recorded (in contrast to the 5-6 in Refs.[38–40]), and the need for assumptions regarding dislocations and planar defects in this method, we simply report on the FWHM and their changes in this work.

2.7 Determination of In Plane Average Lattice Strains

Using the corrected Ni peak positions, nominal x-ray energy and the calibration parameters measured with the LaB_6, the relative average in-plane lattice strains ε_a for Ni reflections at volumes I, II and III were calculated using the following equation:

$$\varepsilon_a = \frac{d_{(hkl)} - d^0_{(hkl)}}{d^0_{(hkl)}} \quad (2)$$

where $d_{(hkl)}$ is the d-spacing averaged over the full detector azimuth (corresponding to the in-plane orientations of the sample), and $d^0_{(hkl)}$ is the first diffraction pattern collected during C4 at

the minimum state of lithiation. Given that strains perpendicular to the detector plane (along the direct beam) were not measured *in operando*, the full strain tensor could not be determined.

3 Results and Discussion

3.1 In Plane Average Lattice Strains

Figure 2 shows the calculated in plane average strain present in the Ni scaffold in Volume III at different degrees of lithiation during cycling, as measured by the Ni (200), (220) and (311) peaks. The average strain calculated is indexed to the crystallographic lattice spacings at the beginning of C4, which corresponds to a minimum degree of lithiation during cycling, and does not take into account any residual strains from processing that would affect the absolute strain state present in the Ni scaffold. Residual processing strains are expected to develop between the Ni_3Sn_2 active layer and the Ni scaffold during the electrodeposition process, which could be either tensile or compressive depending on the specific processing conditions [41–43]. If these residual stresses are tensile, the stresses would counteract lithiation-induced compressive stresses in the scaffold and thus increase the range of strain that the scaffold can elastically accommodate before yielding; the yield strength of the Ni within the scaffold being approximately 600 MPa [44,45]. However, if these stresses are compressive, the lithiation-induced compressive stress that the scaffold is able to elastically accommodate before yielding is lower, and plastic deformation of the Ni may be more significant in the first few cycles.

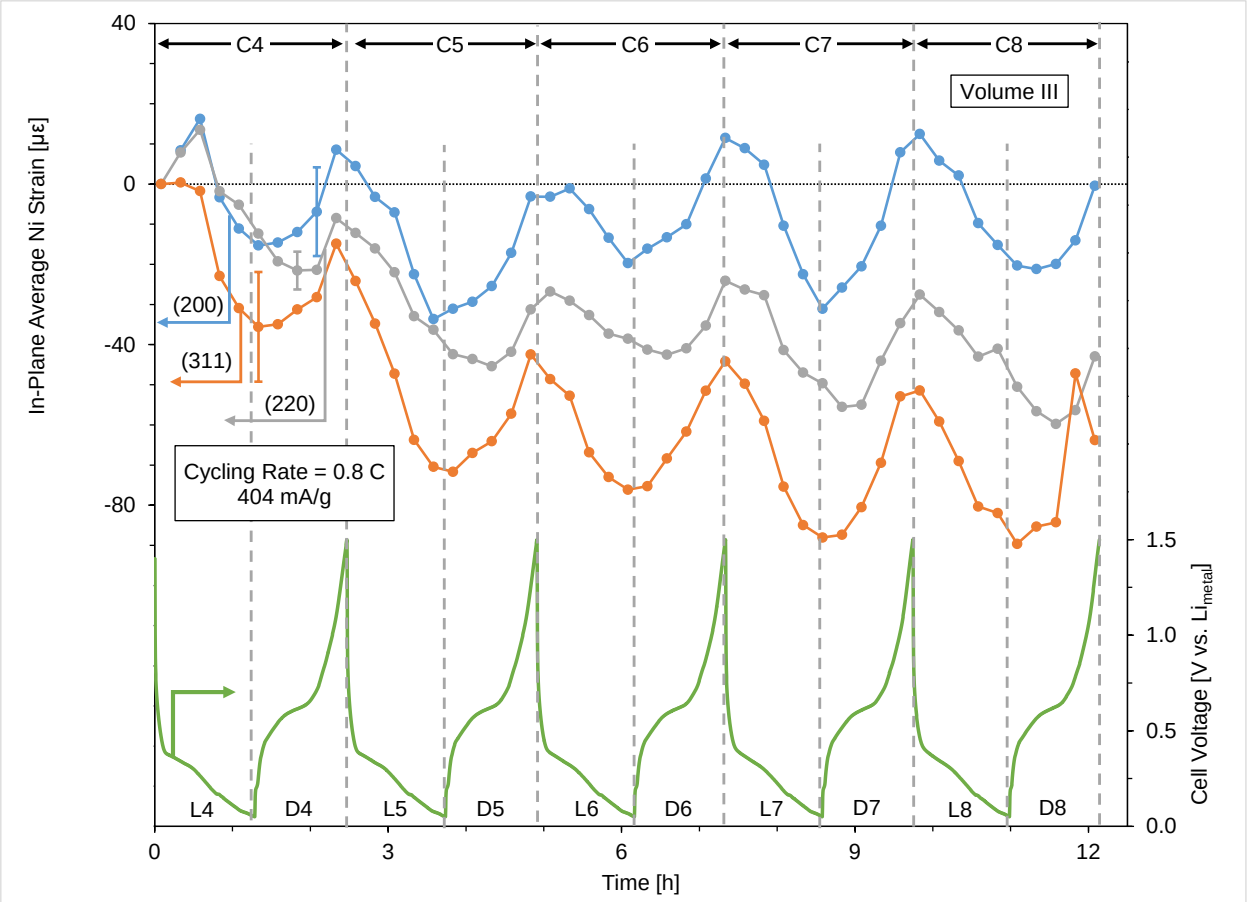

Figure 2: Time-dependence of in-plane average crystallographic strains as measured in volume III in the Ni (200), (220), and (311) diffraction rings (left axis) and electrochemical cell voltage (right axis, V vs. lithium metal counter electrode) (consisting of cycles C4 – C8, where lithiation and delithiation steps in C4 are denoted L4 and D4 respectively, and so on for C5 – C8). A single error bar representative of the estimated uncertainty in pixel fitting and thus strain for each diffraction ring is shown for clarity. The difference in the slopes of the measured crystallographic strains over all of the measured cycles are likely due to slight differences in the instrumental energy drift corrections between the three different volumes.

During lithiation, all three peaks show compressive strains in comparison to the start of C4 during most of each lithiation cycle. All three peaks concomitantly increase with increasing lithiation (and decreasing half-cell voltage) and similarly decrease during delithiation (and increasing half-cell voltage), with strain amplitudes in each peak that appear consistent with cycling. These changes in strain in each peak appear synchronized with each other and the changes in cell voltage across multiple cycles, although curiously, the maximum compressive

strain measured in the Ni (220) in Volume III lags in time relative to the maximum extent of lithiation and other strain measurements during the cycles measured. This discrepancy is not clearly observed in Volume II (Figure S8), and therefore could be within the error of the measurements or caused by inhomogeneity in the scaffold morphology and crystalline orientations between Volumes II and III.

The compressive strains observed in the Ni scaffold during lithiation are due to the expansion of the Ni_3Sn_2 active material. As lithiation progresses, Li^+-ions enter the Ni_3Sn_2 active material and induce expansion preferentially in unconstrained directions, primarily towards the center of the pores present in the inverse opal structure. While expansion of the Ni_3Sn_2 towards the Ni scaffold is also expected to occur, the constraint of the scaffold acts to resist this expansion, thus putting the scaffold into net average compression, which increases as the degree of lithiation increases. This behavior was also observed in our previous experiments with Ni inverse opal supported Si anodes [30] (hereafter referred to as Si anodes). Observed tensile strains (relative to the beginning of C4) suggest that delithiation may not be complete during some of the delithiation steps due to slow diffusion of lithium out of the anode, slow interfacial delithiation processes, or the confined geometry of the Ni_3Sn_2 active material. Figures 3 and 4 compare the calculated in plane average strain in the Ni (200) and (311) peaks, respectively, in volumes I, II and III at different degrees of lithiation during cycling, covering a total sample volume of approximately $7x10^5$ μm^3 for each volume, with approximately 14 layers of inverse opal unit cells through the thickness of the sample, over 200 rows of unit cells along the radius of the beam profile and sampling in total up to 10^6 unit cells. As seen in Figure 2, compressive strain again increases with increasing lithiation and decreases with decreasing lithiation in both peaks and is aligned in time with voltage and thus the state of charge of the anode. This near

perfect temporal alignment suggests that strain and lithiation state do not have relaxation or other non-linear phenomena during cycling at this cycling rate (0.8 C).

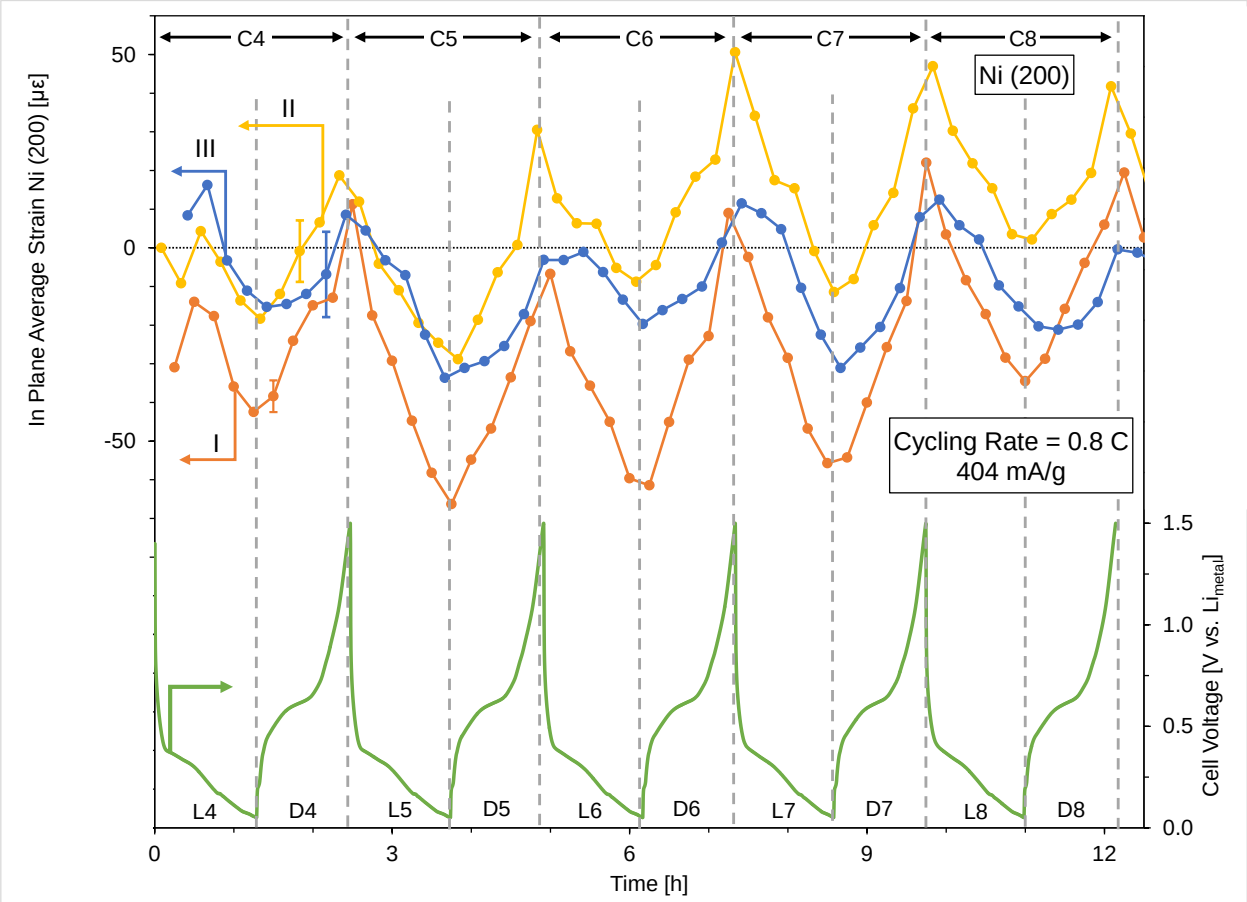

Figure 3: Time-dependence of in-plane average crystallographic strains as measured in the Ni (200) diffraction ring in volumes I, II and III (left axis) and electrochemical cell voltage (right axis, V vs. lithium metal counter electrode) (consisting of cycles C4 – C8, where lithiation and delithiation steps in C4 are denoted L4 and D4 respectively, and so on for C5 – C8). A single error bar representative of the estimated uncertainty in pixel fitting and thus strain for each diffraction ring is shown for clarity.

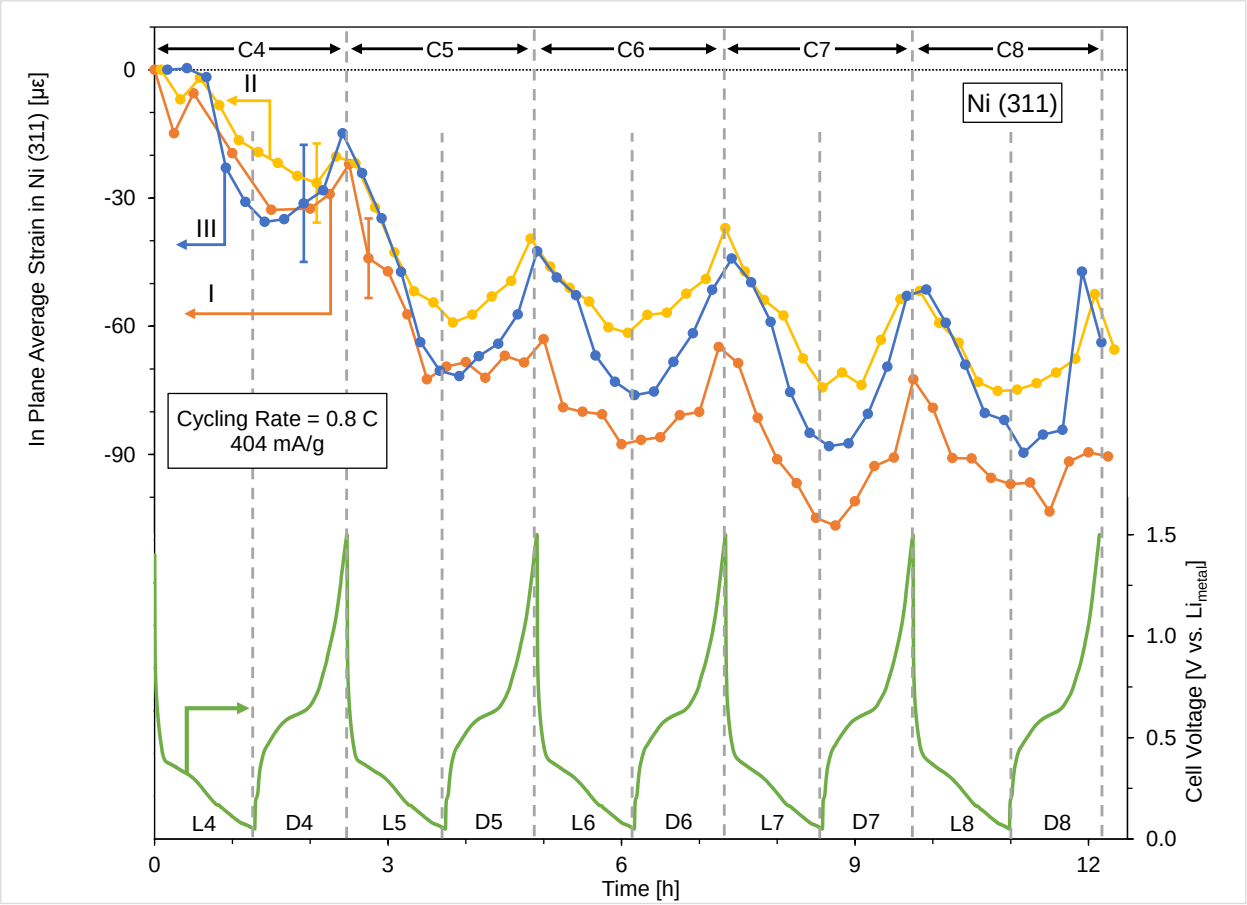

Figure 4: Time-dependence of in-plane average crystallographic strains as measured in the Ni (311) diffraction ring in volumes I, II and III (left axis) and electrochemical cell voltage (right axis, V vs. lithium metal counter electrode) (consisting of cycles C4 – C8, where lithiation and delithiation steps in C4 are denoted L4 and D4 respectively, and so on for C5 – C8). A single error bar representative of the estimated uncertainty in pixel fitting and thus strain for each diffraction ring is shown for clarity.

In both Figures 3 and 4, cycles C6, C7 and C8 have both a similar range of strain and strain rate (or slope of strain over time) measured in the scaffold between the minima and maxima in lithiation for each respective diffraction peak, indicating that the same (de)lithiation-induced strain mechanisms exist between each of these cycles. Additionally, within the temporal resolution and accuracy of our measurements, the slope of the mismatch strains appear linear upon (de)lithiation, suggesting that cycling does not induce major inelastic deformation in the Ni scaffold.

The differences in the strain values between volumes I, II and III are due to inhomogeneity in the scaffold or active layer deposition. However, it is difficult to determine whether changes in the values of each maximum and minimum are due to the build-up of inelastic deformation, though the slopes of the strains suggest linear elastic strain in the scaffold. Additionally, the strains measured in our experiments (and indirectly stresses) only represent strain in two dimensions in the plane of the sample, and thus we are unable to quantify the deviatoric stresses, evaluate von Mises stress criteria or observe the influence of the constraint of the anode substrate on strain in the out-of-plane dimension.

Were plasticity or damage in either the scaffold or the active material, or delamination between the two materials, present in the strain measurements, several key indicators would be present in the strain data. With the onset of plastic deformation, a change in the slope of the strain during (de)lithiation would be observed as increasing strains in the system begin to be accommodated plastically, which is not observed in any of the in plane average strains measured. Delamination and damage would cause a similar change in the slope of the strain, with increasing strains contributing to the propagation of damage as well as increasing elastic strains. Additionally the range of strain travelled during (de)lithiation would decrease as the build-up of inelastic deformation would occur from cycle to cycle and residual stresses would increase in the event of increasing plastic deformation. The maximum and minimum compressive strains during cycling would also change with changes in slope and range of strain, where the buildup of plasticity would induce a ratcheting effect in strain, while delamination and damage would reduce the magnitude of the maximum compressive strains through decreased mismatch strains at higher degrees of lithiation along with decreasing the range of strain travelled. Within error and the accuracy of the fitting, it appears that there are no obvious changes for the mechanical

constraint provided by the scaffold in any cycle in examining either the range of strain or the slopes of the strains. Thus the evolution of lithiation-induced mismatch strain appears to follow the same behavior over multiple points in the anode.

3.2 Peak FWHM and Strain Distribution

Figures 5 and S9 compare the measured in plane average strain with the peak FWHMs for both volumes I and III respectively during cycling. During lithiation of the anode, the FWHM both peaks increases, with the maximum peak width in each cycle corresponding to the maximum state of lithiation as well as the maximum compressive strain observed in that cycle. The increasing FWHM upon lithiation indicates that the distribution of strain within the Ni scaffold is increasing and suggests that a lithiation-induced strain gradient is forming during lithiation. Additionally, as also described in Ref. [30], the geometry of the scaffold may also contribute to an increase in the distribution of strain upon lithiation.

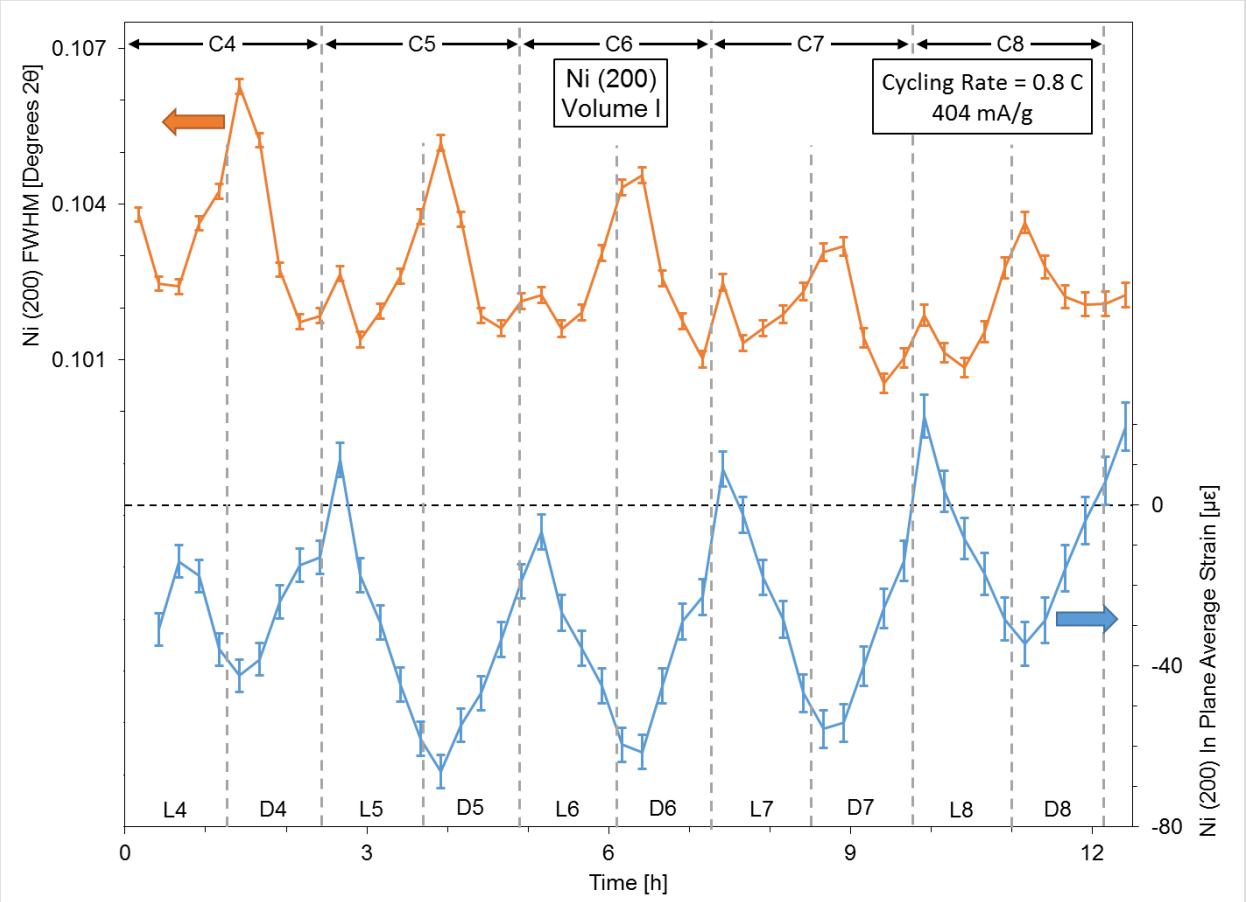

Figure 5: Time-dependence of peak breadth of Ni (200) as measured through the peak Full Width Half Maximum (FWHM, left axis) and in-plane average crystallographic strain in Ni (200) (right axis, as in Figure 3) in volume I (consisting of cycles C4 – C8, where lithiation and delithiation steps in C4 are denoted L4 and D4 respectively, and so on for C5 – C8). The error bars represent the estimated uncertainty in pixel fitting.

The inverse opal scaffold is comprised of a network of nodes connected by struts, which make up 60 and 40% of the Ni volume in the scaffold, respectively. While a uniformly thick coating of Ni_3Sn_2 is expected on the scaffold due to the nature of the electrodeposition process, the coating present on the struts may lithiate more rapidly than the nodes, due to the lower amount of scaffold material relative to the active layer and thus a decreased mechanical constraint from the scaffold. The mechanical constraint of the scaffold, and thus the overall stress state of the coating is expected to affect the diffusion of Li into the Ni_3Sn_2, as has been observed

in other alloying anode systems [46,47]. This decreased mechanical constraint also results in an increase in Li diffusivity in the active material coating the struts, since stress and diffusion are coupled in the active layer, which ultimately causes a preferential lithiation in the struts over the nodes and creates a gradient in lithiation-induced strain in the structure. The strain gradient that forms due to preferential lithiation potentially leads to the accumulation of higher strain values and mismatch strains in the struts than what is achieved in the nodes at equivalent overall degrees of lithiation, which will both broaden the diffraction peaks and increase the average strain in the scaffold.

During delithiation, the minimum FWHM in the Ni (311) peak in vol. III (Figure S9) is observed at or shortly after the minimum degree of lithiation of the anode, suggesting that strain broadening is directly correlated with lithiation in this peak. In contrast, the minimum FWHM in the Ni (200) peak in vol. I (Figure 5) is observed before the minimum degree of lithiation is reached, with a local maximum in broadness occurring at the minimum in lithiation. The presence of these intermediate minima indicate that a balancing between residual strain is occurring at these points, either from potentially tensile strains present after processing or from plastic strain accumulated during cycling of the anode, as was also observed in Ref. [30]. The Ni (311) FWHM extrema (Figure S9) appear to repeatably and reversibly change in response to (de)lithiation of the anode with a similar range of widths between maxima and minima in C4 - C8.

Unlike the behavior seen in the (311), the Ni (200) range of broadness decreases from cycle to cycle (Figure 5), indicating a build-up of inelastic deformation in the scaffold and/or Ni_3Sn_2 layer. A decrease in the range of FWHM indicates that for a similar amount of lithium inserted into the anode, a decrease in the distribution of the strain occurs between cycles, where

completely elastic cycling would have a similar range of peak widths between all cycles shown. Additionally, the values of the minimum FWHM in the (200) are also slightly decreasing from cycle to cycle, indicating that plastic deformation is not significantly occurring in vol. I during cycling, as the accumulation of plastic deformation would be expected to instead increase the minimum and baseline peak breadth [30,48]. The decrease in FWHM instead suggests that the inelastic deformation is caused by damage and delamination build-up in the anode. This damage and delamination could be accelerated by the morphology of the electrodeposited Ni_3Sn_2 active layer, which has some roughness and sharp edges that could serve as stress concentrators and nucleate cracks (see Figures 1 and S1) However, the decreases in the minima from cycle to cycle are slight relative to both the change in maxima and the range of peak broadening observed in any one cycle. Additionally, the contrast between the elastic behavior observed in the volume I (200) (Figure 5) and volume III (311) (Figure S9) diffraction peaks could also indicate that there are significant differences between the strain processes acting on the Ni (100) and (311) planes, due to their different stiffnesses, or that significant differences in the morphology exist between volumes I and III.

3.3 Comparison to Pure a-Si

Figures 6 and S10 show the relative in-plane average strain measured in C4 and C5 using Ni (200) and Ni (311) measurements (respectively), in Volumes I, II and III, in comparison to previous work on amorphous Si inverse opal anodes [30]. Both anodes shown in Figures 6 and S10 have inverse opal scaffolds prepared under identical conditions, with similar scaffold, cell and *in operando* experimental geometries, in addition to their similar lithiation mechanisms [15]. The Si anode was coated onto the inverse opal Ni scaffold using a chemical vapor deposition method, resulting in a much smoother morphology than the Ni_3Sn_2 coating. Since the Sn-based

anode is an intermetallic, as opposed to the pure Si, the total amount of lithiation-induced volume expansion in the Ni_3Sn_2 is expected to be ~100% (as opposed to ~320% for pure Si) [5,15]. Additionally, the cycling rates and temporal resolution of the two experiments are different, with (de)lithiation of Si in Ref. [30] having a slower rate and finer temporal resolution. However, even with these differences, the similarity of the (de)lithiation strain response, combined with relative similarity of the cycling rates between the two anodes, makes the direct comparison of these two cycles useful.

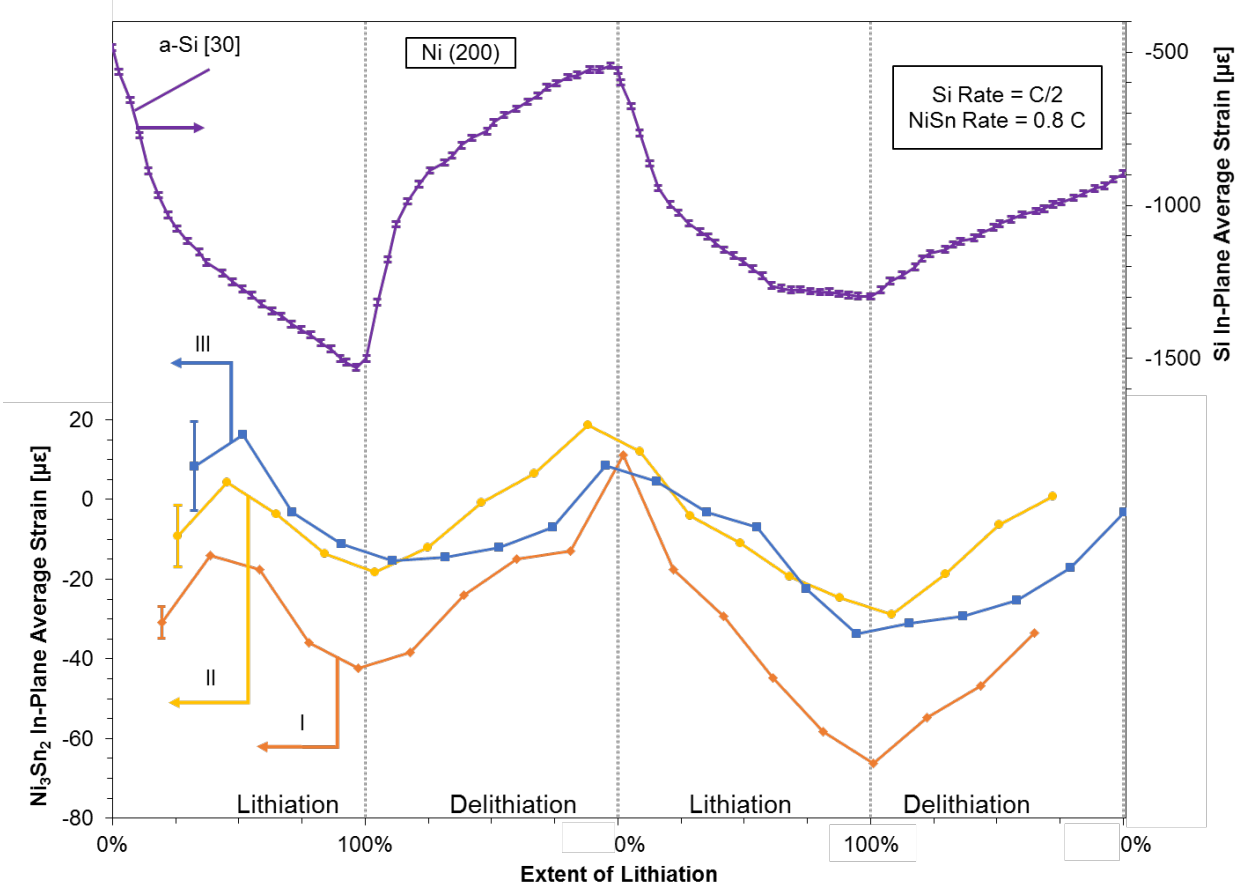

Figure 6: Comparison of the in-plane average crystallographic strain as measured in Ni (200) between Ni_3Sn_2 (left axis) and Si [30] (right axis) inverse opal anodes with respect to the extent of lithiation during each respective cycle. The error bars for the Si anode and a single representative error bar for the Ni_3Sn_2 anode indicate the estimated uncertainty in pixel fitting for each diffraction ring [30].

As seen in the Ni_3Sn_2 anode strain curves, the Si anode's Ni scaffold is subjected to lithiation-induced compressive stresses upon lithiation of the active layer, with decreasing compressive stresses occurring upon delithiation. This behavior is similar to what is observed in Ni_3Sn_2 over two cycles even though the relative and absolute lithiation rates are different, thus confirming that the lithiation mechanisms between the two systems are very similar. During (de)lithiation, the Si anode appears to undergo a two-step lithiation process, as shown by the changes in the slope of the strain curve at intermediate lithiation points. As described by Glazer et al. [30], these changes suggest that plastic deformation and delamination processes are occurring in the Si anode system. The complex changes in slope seen in the Si anode system appear absent from the Ni_3Sn_2 anode system, suggesting that the Ni_3Sn_2 anode has more reversible cyclic strains upon lithiation than the Si anode, although the absence of clear slope changes could also be due in part to the lower temporal resolution of the Ni_3Sn_2 anode measurements in comparison to the Si anode measurements. In addition to the changes in slope, the change in the range of strains traveled during the cycling of these two anodes also appears different, with the relative decrease in the range of strain traveled in the Si anode being much larger than the Ni_3Sn_2 anode. This also suggests that the cycling of the Ni_3Sn_2 anode is more reversible than the Si anode, as a decrease in the range of strain travelled in the Si anode is linked to inelastic deformation processes.

In addition to comparing the average strains, examining the distribution of strains as indirectly measured by peak FWHMs also elucidates important features present in the lithiation behaviors of both the Si and Ni_3Sn_2 anode systems. Figures 7 and S11 compare the FWHMs of the Ni (200) and (311) diffraction peaks, respectively, in the Si and Ni_3Sn_2 anodes. As seen in all peaks for both the Si and Ni_3Sn_2 anodes, an increase in lithiation results in an increase in peak

FWHM and thus an increase in the distribution of strain in each peak, further confirming the similar lithiation mechanisms between the two systems. The range of FWHM changes in the Si anode is an order of magnitude larger than the Ni_3Sn_2 anode for both peaks for very similar experimental setups and sample geometries, similar to what was observed in the average strain comparison for Figures 6 and S10. The difference in the range of FWHMs is similar to the differences in the average strains, again due to the differences in the relative volume expansions between Si and Sn as well as the lower Sn mole fraction in the Ni_3Sn_2 active layer relative to the pure Si active layer.

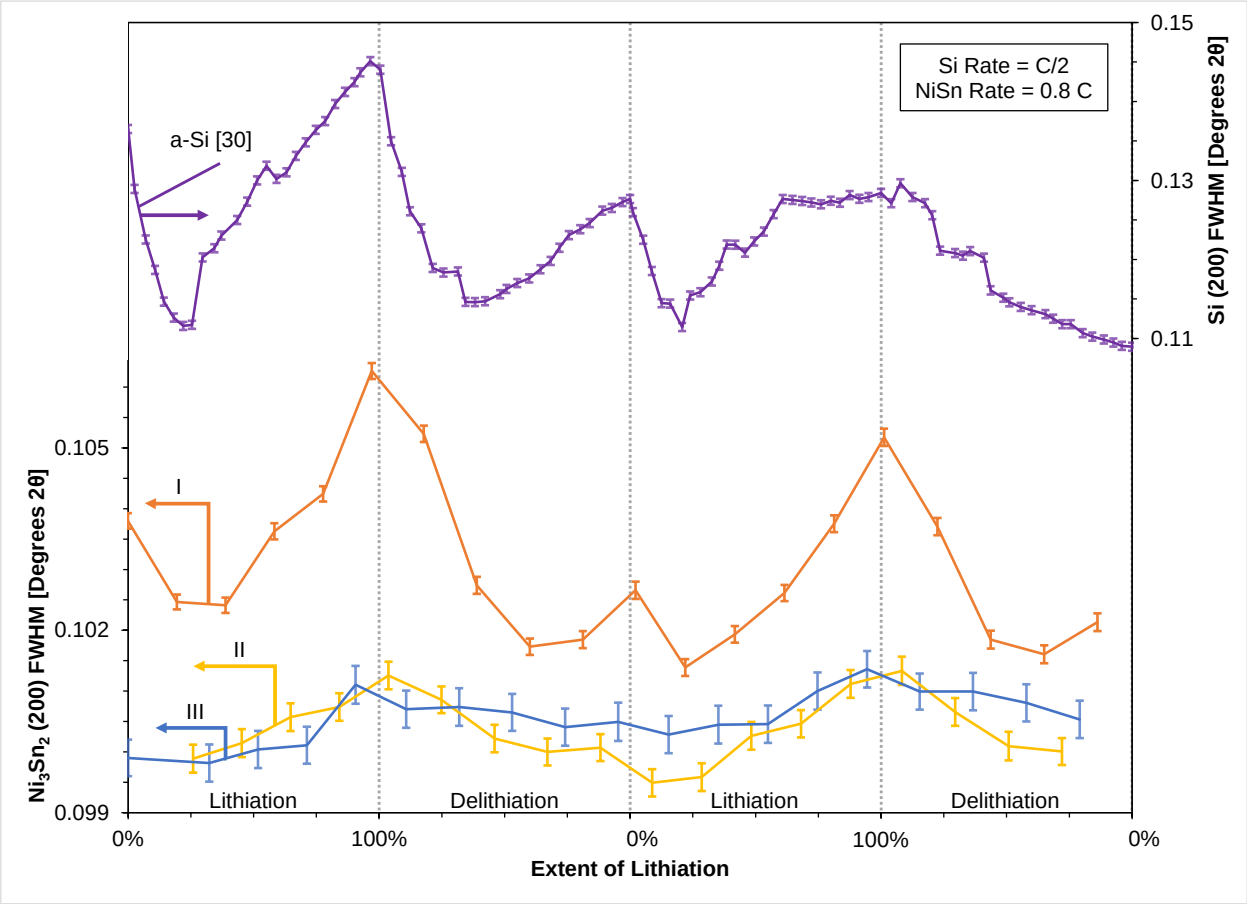

Figure 7: Comparison of the peak breadth measured in Ni (200) between Ni_3Sn_2 (left axis) and Si[30] (right axis) inverse opal anodes with respect to the extent of lithiation during each respective cycle. The error bars for the Si and Ni_3Sn_2 anodes indicate the estimated uncertainty in pixel fitting for each diffraction ring [30].

Unlike what is observed in the average strain and what is observed in the Ni (311) (Figure S10), there are significant differences in the range of FWHM during cycling between Ni_3Sn_2 volumes I, II and III in the Ni (200) diffraction peak (Figure 7). These large differences are likely due to inhomogeneity in the deposition of the Ni_3Sn_2 active layer in the scaffold or differences in the perfection of the Ni inverse opal scaffold itself in the three different volumes, with less perfect scaffold sections having more Ni relative to Ni_3Sn_2 and thus a weaker overall mismatch strain. The differences between the Ni (200) and (311) (Figures 7 and S11) are likely due to the large error in fitting the (311) peak.

In the Ni_3Sn_2 volume I Ni (200), minima in peak breadth are observed at degrees of lithiation, which are between the maximum and minimum degrees of lithiation during cycling, as is also observed in both of the Si peak FWHMs. As also noted by Glazer et al. [30], these intermediate minima suggest the presence of a residual stress distribution present in the scaffold, which is caused either by processing or from the build-up of plastic deformation that occurred during cycling. These intermediate minima may also be present in other Ni_3Sn_2 volumes, but cannot be resolved given the larger uncertainty in fitting for these two volumes.

In examining changes in the range, maxima and minima in the peak FWHM during cycling, the Si anode appears to show a strong decrease in all three values, while no strong changes can be resolved in the Ni_3Sn_2 measurements within error. The decreases in the Si FWHM suggest delamination and damage [30], while the lack of strong changes in Ni_3Sn_2 suggests that the Ni_3Sn_2 anode has a much more reversible cycling behavior with respect to lithiation-induced mismatch strains than the Si anode. While the slopes of both systems FWHMs appear to be mostly linear in between intermediate extrema during cycling, the much lower temporal resolution of the Ni_3Sn_2 measurements makes finer assessment of the slopes of the

FWHMs during cycling more difficult. In combination with average strain analysis, studying changes in the distribution of strain by examining peak breadth allows for a more detailed understanding of lithiation-induced strains in the Ni_3Sn_2 inverse opal anode system, though additional *in operando* characterization and finite element modeling will be necessary to more fully understand the reversibility of the Ni_3Sn_2 anode system, as well as differences in inelastic deformation modes between the Ni_3Sn_2 and Si inverse opal anode systems.

In summary, *in operando* XRD reveals that the lithiation mechanisms in the Ni inverse opal supported Ni_3Sn_2 anode are mostly reversible during cycling for the cycles tested and that these mechanisms are similar to a Ni inverse opal supported Si anode explored in previous studies [30]. While measurement of the average Ni scaffold strains in the Ni_3Sn_2 anode indicated mostly reversible (de)lithiation cycling, the distribution of strains suggested that some inelastic deformation, likely through delamination, may be occurring as well. In comparing the anode studied in this work with the Si anode, both reversible and irreversible lithiation mechanisms appear similar between the two systems, confirming that similar lithiation chemistries also have similar lithiation-induced strain behaviors. However, the Ni_3Sn_2 appeared to undergo much more reversible (de)lithiation behavior, suggesting overall that the Ni inverse opal supported Ni_3Sn_2 anode is more mechanically robust and less prone to damage-induced capacity fade than Ni inverse opal supported Si anodes due to the reduced mismatch stresses and strains associated with the (de)lithiation in the Ni_3Sn_2.

4. Conclusions

Using synchrotron x-ray diffraction-based strain measurements, the lithiation-induced strains in the Ni inverse-opal nanoscaffold coated with active Ni_3Sn_2 were measured *in operando* in three different volumes in the anode. Average strains in the Ni scaffold were measured in a time-

resolved manner during cycling, where the mechanical constraint of the non-lithiating Ni scaffold on the (de)lithiating Ni_3Sn_2 active layer is translated as a lithiation-induced mismatch strain between the two phases. Small elastic strains (ranging from 0 to ca. -80 με) were measured in the scaffold using *in operando* XRD techniques. Additionally, the relatively large volume probed using x-rays allowed for quasi-bulk average strain measurements, which enabled a direct linkage between the electrochemical and mechanical measurements.

The compressive strains, as well as the distribution of strains observed in the Ni scaffold confirm that, even in a very thin nanostructured anode, lithiation is a diffusion-mediated process, which sets up concentration and strain gradients during cycling. The change in peak broadening with (de)lithiation indicates that the average strain and the distribution of strain changes with cycling and points to potential plasticity in the scaffold, as well as delamination between the scaffold and active material. The strain and cycling behavior observed in the Ni inverse opal supported Ni_3Sn_2 anode was very similar to what was observed in our previous work with Ni inverse opal supported amorphous Si anodes [30] and demonstrates that similar mechanisms within the a-Si and Ni_3Sn_2 active layers are likely present during (de)lithiation.

The plasticity, damage and delamination that was inferred in the a-Si anode may also occur in the Ni_3Sn_2 system and will likely have a highly non-uniform influence on the structure. However, an experiment with higher temporal and strain resolution will be necessary to explore plasticity and delamination more fully, where signatures of these inelastic deformation mechanisms may be evident in peak broadening measurements.

Ultimately, understanding and quantifying the effects of mechanical constraints on the mechanics, diffusion and chemical reaction kinetics of the active layer-scaffold anode system is necessary to determine the best constraining strategies for increasing the cycle life of alloying

anodes. Detailed finite element modeling will be necessary to convert the measured strains into a stress-strain map in the Ni nanoscaffold and Ni_3Sn_2 active material, as well as to quantify plasticity and damage in the Ni_3Sn_2 anode system. Overall, our results suggest that inverse opal anodes constrain lithiation and develop lithiation-induced mismatch stresses and strains between the active layer and the mechanically constraining scaffolds, and that both average strains and distributions of strains can be measured experimentally in alloying based anode systems using *in operando* XRD-based measurement techniques.

Acknowledgements

This research was financially supported by the U.S. Department of Energy, Office of Science, Office of Basic Energy Sciences, under Contracts No. DE-AC02-06CH11357 (*in operando* electrochemical and x-ray characterization) and DE-FG02-07ER46471 (*ex situ* electrochemical characterization and electrode fabrication). The authors thank G. Halder (APS) for assistance in Ni_3Sn_2 data collection and the staff of beam line 17-BM of the Advanced Photon Source (ANL) for assistance in experiments and data acquisition. Use of the Advanced Photon Source, an Office of Science User Facility operated for the U.S. Department of Energy (DOE) Office of Science by Argonne National Laboratory, was supported by the U.S. DOE under Contract No. DE-AC02-06CH11357.

References

[1] K. Amine, R. Kanno, Y. Tzeng, MRS Bull. 39 (2014) 395.

[2] T.S. Arthur, D.J. Bates, N. Cirigliano, D.C. Johnson, P. Malati, J.M. Mosby, E. Perre, M.T. Rawls, A.L. Prieto, B. Dunn, MRS Bull. 36 (2011) 523.

[3] J.M. Tarascon, M. Armand, Nature 414 (2001) 359.

[4] M.S. Whittingham, Proc. IEEE 100 (2012) 1518.

[5] W.-J. Zhang, J. Power Sources 196 (2011) 13.

[6] M.-K. Song, S. Park, F.M. Alamgir, J. Cho, M. Liu, Mater. Sci. Eng. R Reports 72 (2011) 203.

[7] M.T. McDowell, S.W. Lee, W.D. Nix, Y. Cui, Adv. Mater. 25 (2013) 4966.

[8] C. Jiang, E. Hosono, H. Zhou, Nano Today 1 (2006) 28.

[9] M. Osiak, H. Geaney, E. Armstrong, C. O'Dwyer, J. Mater. Chem. A 2 (2014) 9433.

[10] A. Vu, Y.Q. Qian, A. Stein, Adv. Energy Mater. 2 (2012) 1056.

[11] L. Xu, C. Kim, A.K. Shukla, A. Dong, T.M. Mattox, D.J. Milliron, J. Cabana, Nano Lett. 13 (2013) 1800.

[12] R.A. Huggins, J. Power Sources 81-82 (1999) 13.

[13] G.M. Ehrlich, C. Durand, X. Chen, T.A. Hugener, F. Spiess, S.L. Suib, J. Electrochem. Soc. 147 (2000) 886.

[14] J.-H. Ahn, G.X. Wang, J. Yao, H.K. Liu, S.X. Dou, J. Power Sources 119-121 (2003) 45.

[15] W.-J. Zhang, J. Power Sources 196 (2011) 877.

[16] M.N. Obrovac, L. Christensen, D.B. Le, J.R. Dahn, J. Electrochem. Soc. 154 (2007) A849.

[17] A. Mukhopadhyay, R. Kali, S. Badjate, A. Tokranov, B.W. Sheldon, Scr. Mater. 92 (2014)

47.

[18] J. Chen, S.J. Bull, S. Roy, H. Mukaibo, H. Nara, T. Momma, T. Osaka, Y. Shacham-Diamand, J. Phys. D. Appl. Phys. 41 (2008) 025302.

[19] X.H. Liu, J.Y. Huang, Energy Environ. Sci. 4 (2011) 3844.

[20] L.Y. Beaulieu, S.D. Beattie, T.D. Hatchard, J.R. Dahn, J. Electrochem. Soc. 150 (2003) A419.

[21] S.-C. Chao, Y.-C. Yen, Y.-F. Song, H.-S. Sheu, H.-C. Wu, N.-L. Wu, J. Electrochem. Soc. 158 (2011) A1335.

[22] S.-C. Chao, Y.-F. Song, C.-C. Wang, H.-S. Sheu, H.-C. Wu, N.-L. Wu, J. Phys. Chem. C 115 (2011) 22040.

[23] S.-C. Chao, Y.-C. Yen, Y.-F. Song, Y.-M. Chen, H.-C. Wu, N.-L. Wu, Electrochem. Commun. 12 (2010) 234.

[24] M. Ebner, F. Marone, M. Stampanoni, V. Wood, Science (80-.). 342 (2013) 716.

[25] A. Mukhopadhyay, B.W. Sheldon, Prog. Mater. Sci. 63 (2014) 58.

[26] J.Y. Huang, L. Zhong, C.M. Wang, J.P. Sullivan, W. Xu, L.Q. Zhang, S.X. Mao, N.S. Hudak, X.H. Liu, A. Subramanian, H. Fan, L. Qi, A. Kushima, J. Li, Science (80-.). 330 (2010) 1515.

[27] M.L. Young, J. DeFouw, J.D. Almer, D.C. Dunand, Acta Mater. 55 (2007) 3467.

[28] J.D. Almer, S.R. Stock, J. Struct. Biol. 152 (2005) 14.

[29] C. Weyant, J.D. Almer, K. Faber, Acta Mater. 58 (2010) 943.

[30] M.P.B. Glazer, J. Cho, J. Almer, J. Okasinski, P. V. Braun, D.C. Dunand, Adv. Energy Mater. 5 (2015) n/a.

[31] R. Hu, M. Zhu, H. Wang, J. Liu, O. Liuzhang, J. Zou, Acta Mater. 60 (2012) 4695.

[32] D.E. Conte, M. Mouyane, L. Stievano, B. Fraisse, M.T. Sougrati, J. Olivier-Fourcade, P. Willmann, C. Jordy, M. Artus, S. Cassaignon, K. Driezen, J.-C. Jumas, J. Solid State Electrochem. 16 (2012) 3837.

[33] Y.S. Lin, J.G. Duh, H.S. Sheu, J. Alloys Compd. 509 (2011) 123.

[34] M. Sougrati, J. Fullenwarth, A. Debenedetti, J. Mater. Chem. (2011) 10069.

[35] J.H. Pikul, H. Gang Zhang, J. Cho, P. V Braun, W.P. King, Nat. Commun. 4 (2013) 1732.

[36] A.P. Hammersley, S.O. Svensson, A. Thompson, H. Graafsma, A. Kvick, J.P. Moy, Rev. Sci. Instrum. 66 (1995) 2729.

[37] Hammersley, ESRF Intern. Rep. ESRF98HA01 (1998).

[38] M. Fares, M.Y. Debili, E-Journal Surf. Sci. Nanotechnol. 6 (2008) 258.

[39] V. Soleimanian, M. Mojtahedi, Appl. Phys. A 119 (2015) 977.

[40] T. Ungár, I. Dragomir, Á. Révész, A. Borbély, J. Appl. Crystallogr. 32 (1999) 992.

[41] F. Ebrahimi, Q. Zhai, D. Kong, Scr. Mater. 39 (1998) 315.

[42] A.M. El-Sherik, J. Shirokoff, U. Erb, J. Alloys Compd. 389 (2005) 140.

[43] S.E. Hadian, D.R. Gabe, Surf. Coatings Technol. 122 (1999) 118.

[44] W.M. Haynes, T.J. Bruno, D.R. Lide, eds., Handbook of Chemistry and Physics, 95th ed., CRC Press Inc., 2000 Corporate Blvd. NW, Boca Raton, FL 33431, 2014.

[45] F. Ebrahimi, G.R. Bourne, M.S. Kelly, T.E. Matthews, Nanostructured Mater. 11 (1999) 343.

[46] A.F. Bower, P.R. Guduru, V.A. Sethuraman, J. Mech. Phys. Solids 59 (2011) 804.

[47] A.F. Bower, P.R. Guduru, Model. Simul. Mater. Sci. Eng. 20 (2012) 045004.

[48] I.C. Noyan, J.B. Cohen, Mater. Sci. Eng. 75 (1985) 179.